nature communications

Article

https://doi.org/10.1038/s41467-024-55666-0

Regulation of stress granule maturation and dynamics by poly(ADP-ribose) interaction with PARP13

Received: 12 June 2024

Accepted: 19 December 2024

Published online: 13 January 2025

Check for updates

Shang-Jung Cheng[1], Temitope Gafaar[1], Jijin R. A. Kuttiyatveetil[2], Aleksandr Sverzhinsky[2], Carla Chen[1], Minghui Xu[1], Allison Lilley[1], John M. Pascal[2] & Anthony K. L. Leung[1,3,4,5]

Non-covalent interactions of poly(ADP-ribose) (PAR) facilitate condensate formation, yet the impact of these interactions on condensate properties remains unclear. Here, we demonstrate that PAR-mediated interactions through PARP13, specifically the PARP13.2 isoform, are essential for modulating the dynamics of stress granules—a class of cytoplasmic condensates that form upon stress, including types frequently observed in cancers. Single amino acid mutations in PARP13, which reduce its PAR-binding activity, lead to the formation of smaller yet more numerous stress granules than observed in the wild-type. This fragmented stress granule phenotype is also apparent in PARP13 variants with cancer-associated single-nucleotide polymorphisms (SNPs) that disrupt PAR binding. Notably, this fragmented phenotype is conserved across a variety of stresses that trigger stress granule formation via diverse pathways. Furthermore, this PAR-binding mutant diminishes condensate dynamics and impedes fusion. Overall, our study uncovers the important role of PAR-protein interactions in stress granule dynamics and maturation, mediated through PARP13.

Stress granules are cytoplasmic biomolecular condensates that form in cells that encounter environmental challenges[1–5]. The granules are composed of untranslated mRNAs, translation initiation factors, such as eIF3b, and RNA-binding proteins that dissociate from polysomes[6,7]. Stress granules are formed when translation initiation is inhibited, a process commonly mediated by the phosphorylation of the translation factor eIF2α or by inhibiting eIF4A functions[8]. These condensates are proposed to remodel the cellular transcriptome during stress and sequester cell death-related signaling molecules[1–4]. Stress granules have also been implicated in multiple diseases, including viral infection, cancer, and neurodegeneration[1–5]. Therefore, gaining insights into stress granule assembly and disassembly could lead to a better understanding of these diseases and shed light on new therapeutic approaches.

Stress granules are highly dynamic and show characteristics of a liquid-like state[9–12], supported by the rapid exchange of proteins with their surroundings. Stress granules evolve dynamically during assembly, starting small and growing to mature sizes through fusion[13]. After removal of the stress trigger, they are disassembled[14,15]. Super-resolution imaging has revealed the non-uniform distribution of the core components G3BP1 and UBAP2L within stress granules[13,16–18]. This observation aligns with the current assembly model linking stable cores via molecular interactions[6,13,16]. Interfering with these interactions, e.g., by inhibiting G3BP1 dimerization, reduces stress granule formation[19,20].

[1]Department of Biochemistry and Molecular Biology, Bloomberg School of Public Health, Johns Hopkins University, Baltimore, MD, USA. [2]Department of Biochemistry and Molecular Medicine, Université de Montréal, Montréal, QC, Canada. [3]Department of Molecular Biology and Genetics, Johns Hopkins University, Baltimore, MD, USA. [4]McKusick-Nathans Department of Genetic Medicine, Johns Hopkins University, Baltimore, MD, USA. [5]Department of Oncology, School of Medicine, Johns Hopkins University, Baltimore, MD, USA. e-mail: anthony.leung@jhu.edu

Notably, disease-associated mutations of stress granule components can lead to changes in the biophysical properties of the granules through a liquid-to-solid transition[3,11,21,22]. This type of transition is implicated as a possible mechanism for forming pathological aggregates in neurodegenerative diseases[3,11,21,22]. Yet, the mechanisms that control the physical properties of stress granules and regulate their size, maturation, and dynamics remain largely undefined.

Work from us and others has revealed that poly(ADP-ribose) (PAR), a nucleic acid-like polymer that is synthesized by ADP-ribosyltransferases (aka PARPs), is an important component of stress granules[23–26]. PAR serves as a multivalent scaffold[27,28] and plays a pivotal role in the structural integrity of these granules[23–25]. PAR's precise function and potential impact on stress granule dynamics remain incompletely understood partly because how PAR interacts within remains unclear.

In this work, we established that the stress granule-associated PARP13, specifically the shorter PARP13.2 isoform, can modulate the dynamics and physical properties of stress granules. Among the five PARPs localized with stress granules, PARP13 is unique because it lacks ADP-ribosyltransferase activity, yet it binds to PAR[29,30]. By investigating mutations in the PAR-binding domain, we identified the role of PARP13 in maintaining the liquid-like state of stress granules. Expression of these dominant-negative PARP13 mutants resulted in slower stress granule dynamics, impaired fusion, and the formation of smaller yet more numerous stress granules.

Results

The PAR-binding function of PARP13 is critical in regulating stress granule size and number

Following up on the identification of various PARPs in stress granules[23], we noticed that although the number of stress granules remained similar, those in PARP13 knockout HeLa cells were smaller compared to those in wild-type cells under arsenite stress (Fig. 1A, B). To systematically determine the domain crucial for granule size, we reintroduced PARP13 constructs into the knockout cells to identify which one could rescue the phenotype. PARP13 possesses two major isoforms: PARP13.1 and PARP13.2, with the latter lacking the ADP-ribosyltransferase (ART) domain typical of all PARPs (Fig. 1C). Compared to PARP13.2, PARP13.1 exhibited significantly lower colocalization with stress granules (Fig. 1A), consistent with their established localizations and roles in the endoplasmic reticulum[31–33]. More critically, while transfection of PARP13.1 in PARP13 knockout cells did not rescue the stress granule size (Fig. S1A), transfection of PARP13.2 restored both the mean and total area of stress granules per cell to levels observed in wild-type cells (Fig. 1A, B). These data indicate that expressing the shorter isoform—the focus of this study—is sufficient to compensate for the loss observed in the knockout phenotype.

To further delineate the specific contributions of each remaining domain of PARP13, we then created different deletion mutants and examined their effects in HeLa cells (Figs. 1C, D and S1B). Consistent with prior studies investigating the interactions of PARP13 with RNA and stress granules[34], the N-terminal half of PARP13 (ΔC), which contains the four RNA-binding zinc fingers, was sufficient for stress granule localization (Fig. 1C, D). Mutations of residues that are responsible for zinc coordination[35] or RNA binding[32] led to a complete or partial loss of stress granule localization, respectively (Fig. S1C, D). Unexpectedly, the C-terminal fragments of PARP13.2, including those with tandem WWE domains and a zinc finger (ΔN and ZnF5-WWE1&2), and even just the second WWE domain (WWE2), were sufficient to localize to stress granules (Fig. 1D). Therefore, domains at both N- and C-termini of PARP13 play a critical role in stress granule localization—with the N-terminus likely mediating through its ability to bind RNA, but the role of the C-terminus remains unclear.

Recent biochemical and structural analyses of PARP13 revealed that the second WWE domain near the C-terminus specifically binds to the 2′ terminus of PAR, with binding sites that extend along a positively charged groove on the surface, accommodating the preceding polymeric ADP-ribose units ("PAR path"; Fig. 1E)[29,30]. Prompted by these findings, we aimed to investigate the role of PAR binding by PARP13 in stress granule formation. To identify essential PAR-binding residues in the second WWE domain of PARP13, we aligned it with the well-characterized PAR-binding WWE domain of RNF146[36], identifying two conserved amino acids (Y659 and Q668) that likely interact with ADP-ribose (Fig. S1E). We then mutated these residues to alanine in the ZnF5-WWE1&2 fragment and assessed the mutants' PAR-binding capacity in vitro. Using fluorescently labeled 20-mer PAR, we measured the dissociation constants for both wild-type and mutant fragments via fluorescence polarization, revealing that mutations Y659A and Q668A significantly decreased PAR binding (Fig. S1F). Notably, even with these mutations, PARP13.2 still localized to stress granules in HeLa cells under arsenite stress, suggesting PAR-binding is not the sole determinant for PARP13 localization (Fig. 1F), consistent with our finding that the N-terminus also plays a critical role for stress granule localization (Fig. 1D).

Interestingly, HeLa cells transiently expressing these mutants exhibited a "fragmented" phenotype, characterized by a greater number of stress granules that were significantly smaller than the wild-type (Fig. 1F, G). This observation was not due to expression levels (Fig. S2A) or specific to a particular cell type, as similar phenotypes were also observed in U2OS cells (Fig. S2B, C). Further investigation revealed a similar fragmented stress granule phenotype in another recently identified PAR-binding mutant W611A[29,30], (Fig. S2D, E) where the tryptophan residue engages one face of the adenine base of the terminal ADP-ribose within the WWE2 domain (Fig. 1E). These findings collectively indicated that the fragmented stress granule phenotype may stem from reduced PAR-binding by PARP13.2, highlighting the critical role of PAR binding in stress granule size regulation.

Among these mutants, the Y659A mutant exhibited the most pronounced phenotype, with the tyrosine residue forming a hydrogen bond with the terminal ADP-ribose in the WWE2 domain (Fig. 1E). For these reasons, it was selected as our model mutant for subsequent analyses. Notably, this mutant displayed stress granules significantly smaller in size (Fig. 1F, G)—a characteristic that closely mirrors the phenotype observed in PARP13 knockout cells (Fig. 1A, B) albeit with a subtle difference: this mutant generated a greater number of granules than the knockout cells and when the total areas of the stress granules were summed, they were equivalent to those of the wild-type. Observing the "fragmented" phenotype in cells expressing endogenous PARP13 (Fig. 1F, G) suggests a potential dominant-negative effect from PAR-binding deficient mutants, likely due to its ability to dimerize with endogenous PARP13[35]. However, this phenotype was also observed in PARP13 knockout cells transfected with Y659A, indicating that it can occur without the wild-type protein (Fig. S2F, G). More importantly, this PAR-binding deficient mutant failed to rescue the reduced granule size in PARP13 knockout cells (Fig. S2G). Taken together, these data suggest that the PAR-binding activity of PARP13 is critical for regulating the number and size of stress granules.

PARP13 PAR-binding deficiency: no impact on key stress granule components or associated translation processes

To address whether the smaller condensates formed by the PAR binding-deficient mutant Y659A are genuine stress granules, we investigated their composition. In addition to the canonical stress granule marker eIF3b, we examined seven other stress granule markers using immunofluorescence microscopy. These markers included the

https://doi.org/10.1038/s41467-024-55666-0

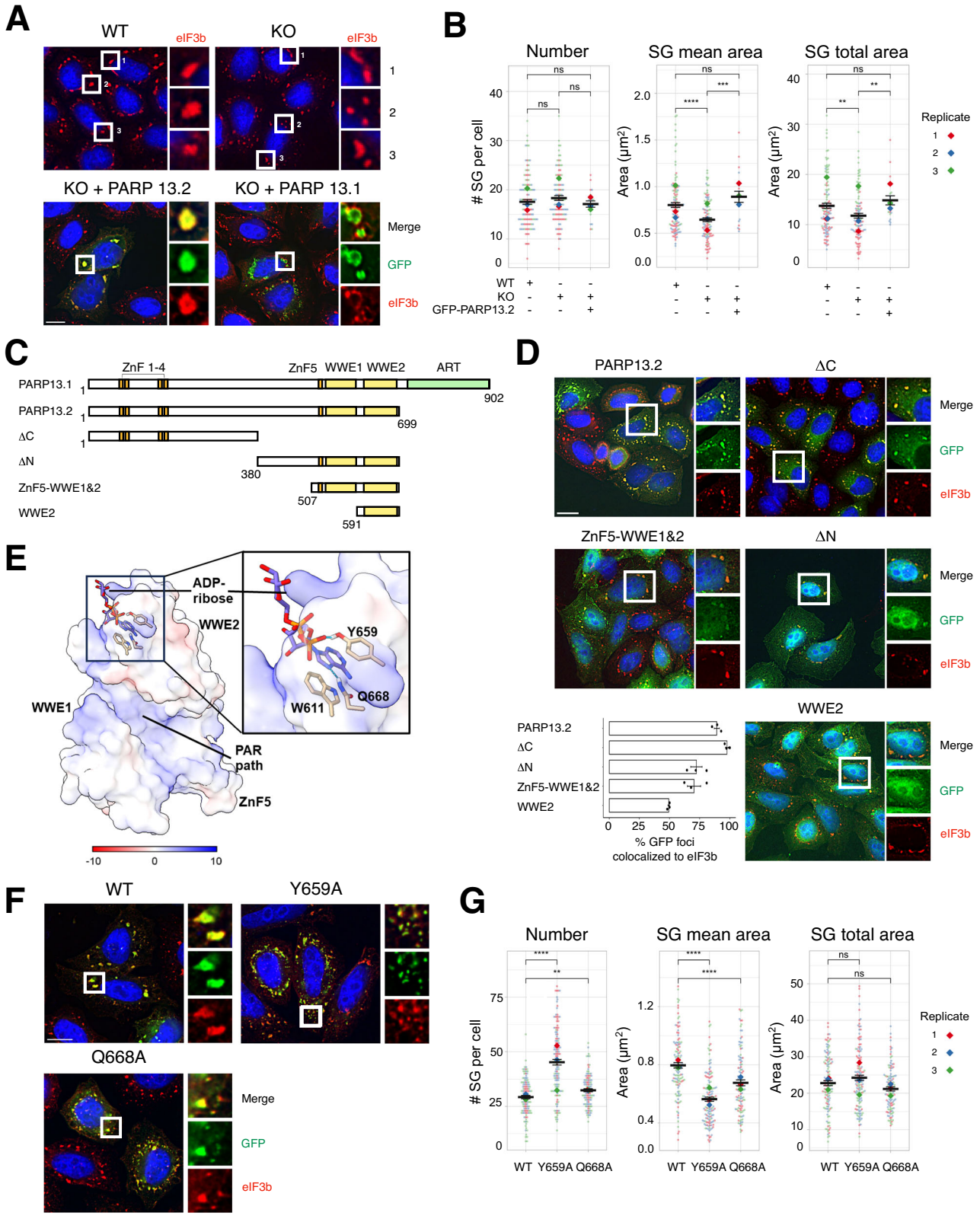

two core components G3BP1 and UBAP2L[16,18], two other RNA-binding proteins (TIA1 and HuR), and three translation initiation factors (eIF4A, eIF4E, and eIF4G). In all cases, the smaller condensates formed upon Y659A expression contained the same components as wild-type stress granules (Fig. 2A). Additionally, the expression levels of key stress granule proteins, such as G3BP1, UBAP2L, and CARPIN1, were comparable between cells expressing either the wild-type or Y659A mutant (Fig. S3A). These findings indicate that the smaller size of granules in cells expressing the PAR-binding mutant is not due to a loss of any of the tested proteins.

One hallmark of stress granules is their sensitivity to the translation elongation inhibitor cycloheximide. This inhibitor triggers stress granule disassembly by trapping mRNAs and translation factors in polysomes, thereby reducing their availability for granule formation[15].

Fig. 1 | PAR-binding ability of PARP13.2 is critical for maintaining stress granule size. A HeLa wild-type (WT), PARP13 knockout (KO) cells, and KO cells expressing GFP-PARP13.1 and PARP13.2 were treated with 100 μM sodium arsenite for 1 h. Cells were fixed and stained for eIF3b (red) and DAPI (blue) for stress granule analysis. Transfected cells were shown in green. Scale bar, 10 μm. **B** Stress granule number, mean area, and total area in panel **A** were quantified by ImageJ. The mean ± s.e. of each parameter was reported from three biological replicates; $^{**}p < 0.01$, $^{***}p < 0.001$, $^{****}p < 0.0001$, ns = not significant, two-tailed unpaired Mann–Whitney U test for SG number analysis and two-tailed unpaired Student's *t* test for the rest. Number of cells analyzed was provided in Source data. **C** Diagram of full-length and truncated forms of PARP13. **D** Wild-type HeLa cells expressing GFP-tagged full-length or truncated PARP13.2 constructs were treated with 250 μM sodium arsenite for 30 min. Cells were fixed and stained for eIF3b (red) and DAPI (blue). Transfected cells were shown in green. The percentage of GFP foci localized to eIF3b in transfected cells was used to measure stress granule colocalization. The bar graph indicates the percentage of mean ± s.e. from three biological replicates. Scale bar, 10 μm. Number of cells analyzed was provided in Source data. **E** Terminal ADP-ribose binding cavity of PARP13 (PDB: 7TGQ) with key residues highlighted. **F** Wild-type HeLa cells expressing GFP-tagged wild-type PARP13.2 or mutants were treated with 100 μM sodium arsenite for 1 h. Cells were fixed and stained for eIF3b (red) to visualize stress granules. DAPI (blue) was used for nuclei staining. Transfected cells were shown in green. Scale bar, 10 μm. **G** Quantification of panel **F**. GFP channel was used for analyzing stress granule number, mean area, and total area. The mean ± s.e. of each parameter was reported from three biological replicates; $^{**}p < 0.01$, $^{****}p < 0.0001$, ns = not significant, two-tailed unpaired Mann-Whitney U test for SG number analysis and two-tailed unpaired Student's *t* test for the rest. Number of cells analyzed was provided in Source data.

The smaller condensates formed by the Y659A mutant were sensitive to cycloheximide (Fig. 2B), further confirming that they are bona fide stress granules.

Stress granule formation is a multistep process dependent on translation inhibition, which can be triggered by phosphorylation of eIF2α (e.g., upon arsenite treatment). We, therefore, wondered whether the stress granule phenotype that we observed could be due to altered eIF2α phosphorylation. However, we observed no differences in eIF2α phosphorylation between wild-type and Y659A mutant-expressing cells (Fig. S3B). As stress granule formation is linked to translation[8], we also examined if the expression of wild-type or the Y659A mutant affects global protein translation. Using puromycin to label and release elongating polypeptide chains from translating ribosomes, we determined that translation levels remain comparable between cells expressing the wild-type PARP13 or the Y659A mutant. The same is observed for arsenite-induced translation inhibition (Fig. S3C). Therefore, we conclude that the PAR-binding activity of PARP13 is not required for eIF2α phosphorylation upon stress and does not affect cellular translation.

Restoration of stress granule size requires specific PAR-binding domains

The smaller stress granule size in cells expressing the Y659A mutant could instead be due to its inability to bind and retain PAR in stress granules. Nonetheless, stress granules in cells expressing either the wild-type or the Y659A mutant were positively stained for PAR using three different antibodies (Figs. 2C, and S3D), indicating that the reduced size of these granules is not due to a lack of PAR.

Given that PAR remains present in the smaller granules, we hypothesized that reintroducing a functional PAR-binding unit in the PARP13 Y659A mutant could restore its PAR-binding affinity, potentially rescuing the fragmented stress granule phenotype. To test this hypothesis, we engineered chimera constructs adding either a known PAR-binding fragment (the fifth ZnF and two WWE domains; ZnF5-WWE1&2)[30], the second WWE domain alone (structurally confirmed to bind PAR[29,30]; WWE2), or the established PAR-binding RNF146 WWE domain[36] to the Y659A mutant's C-terminus (Figs. 2D, and S3E). The number of stress granules decreased in all cases compared to the Y659A mutant alone, but it remained higher than for the wild-type (Fig. 2E, F).

Stress granule size was also partially restored in the presence of ZnF5-WWE1&2 or WWE2 of PARP13 (Fig. 2E, F). Interestingly, even though the RNF146 WWE domain binds PAR, adding it to the C-terminal of the Y659A PARP13.2 mutant did not restore stress granule size (Fig. 2E, F). While both the PARP13 and RNF146 WWE domains bind to PAR, they exhibit distinct specificity: the PARP13 WWE domain prefers the 2′ terminus of PAR, while the RNF146 WWE domain recognizes the *iso*-ADP-ribose unit bridging between PAR[30,36]. Taken together, these data suggest that both the specificity of the PAR interaction and the position of the PAR-binding domain within PARP13 are critical factors influencing stress granule size.

Chemical inhibition of stress granule-associated PAR synthesis recapitulates the fragmented phenotype of the PARP13 PAR-binding mutant

To determine if the fragmented stress granule phenotype observed upon expression of PARP13 PAR-binding mutants is indeed dependent on the loss of PAR interaction, we treated PARP13 knockout cells expressing either wild-type PARP13.2 or the Y659A mutant with PARP inhibitors. Our hypothesis was that inhibiting PAR synthesis would recapitulate the fragmented stress granule phenotype in knockout cells reconstituted with the wild-type, but it should not have an impact on cells expressing the PAR-binding mutant.

Among the stress granule-associated PARPs, only PARP5a adds PAR, while others are either catalytically inactive, such as PARP13, or limited to adding only single ADP-ribose units[23,37]. Therefore, we tested how the size and number of stress granules are affected by G007-LK, which inhibits PARP5a and its orthologue PARP5b[38]. Inhibition of these cytoplasmic PARPs reduced the size and increased the number of stress granules in knockout cells reconstituted with wild-type PARP13.2 (Fig. 3A, B). However, in cells expressing the Y659A mutant, the inhibition did not further alter the already increased number and reduced size of stress granules (Fig. 3A, B). These observations were consistent across other PARP5a/b inhibitors (XAV939, TA91, and TA92; Fig. S4A, B), and the efficacy of the inhibition was demonstrated by the increase in the PARP5a/b level[39,40] (Fig. S4C). In contrast, Olaparib (which inhibits PARP1 or PARP2, both localized in the nucleus) did not affect the number and size of stress granules in knockout cells reconstituted with wild-type PARP13 or the Y659A mutant (Fig. 3A, B). Moreover, treating wild-type HeLa cells with G007-LK induced a greater number of smaller-sized stress granules—an effect not observed in PARP13 knockout cells (Fig. S4D, E), indicating this fragmented phenotype requires the presence of PARP13.2. Olaparib, again, had no impact on this process (Fig. S4D, E). Taken together, these data indicate that cytoplasmic PAR is critical for the regulation of stress granule size, mediated at least in part through the PAR-binding WWE domains of PARP13.

The fragmented phenotype induced by PARP13 PAR-binding mutant is independent of stress triggers

To investigate whether this fragmented phenotype is specific to arsenite stress, we also treated PARP13 knockout cells transfected with either wild-type PARP13.2 or the Y659A mutant with various stressors that trigger eIF2α phosphorylation, including osmotic stress using NaCl and mitochondrial stress using clotrimazole, as well as two inhibitors targeting the translational initiator eIF4A, hippuristanol and pateamine A[7]. Across all tested stress conditions, cells expressing the PAR-binding deficient mutant Y659A

https://doi.org/10.1038/s41467-024-55666-0

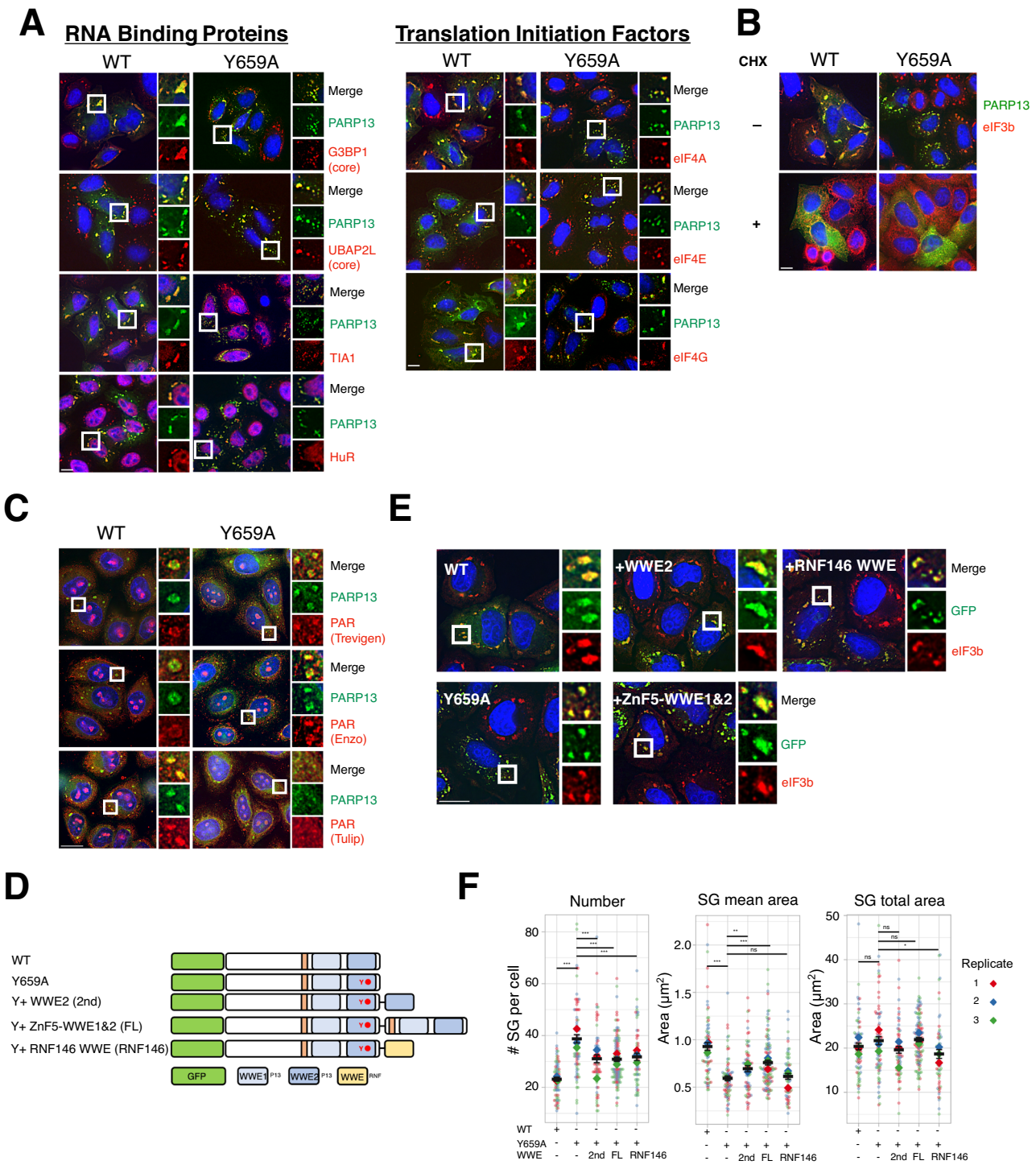

Fig. 2 | Comparative analysis of stress granules from cells expressing wild-type PARP13 and PAR-binding mutant. A HeLa PARP13 knockout cells expressing GFP-tagged WT-PARP13.2 or Y659A mutant were treated with 100 μM sodium arsenite for 1 h. Cells were fixed and stained for the indicated antibodies (red) and DAPI (blue). Transfected cells were shown in green. Scale bar, 10 μm. Representative images were selected from three biological replicates. **B** HeLa PARP13 knockout cells expressing GFP-tagged WT-PARP13.2 or Y569A mutant were treated with 100 μM sodium arsenite for 1 h. Additionally, cells were co-treated with 100 μg/mL cycloheximide with sodium arsenite for 1 h to trigger stress granule disassembly. Cells were fixed and stained for eIF3b (red) and DAPI (blue) for stress granule analysis. Transfected cells were shown in green. Scale bar, 10 μm. Results were obtained from three independent replicates, and representative images were selected. **C** HeLa GFP knock-in CRISPR wild-type and Y659A mutant cells were treated with 250 μM sodium arsenite for 1 h (see later sections for characterization). Cells were fixed and stained for three PAR antibodies (red) and DAPI (blue) as indicated. Endogenous PARP13 was shown in green. Scale bar, 10 μm. Representative images were selected from two (Enzo and Tulip) to three (Trevigen) biological replicates. **D** Schematics of Y659A chimera constructs. **E** Wild-type HeLa cells expressing GFP-tagged wild-type PARP13.2, Y659A, or chimera mutants were treated with 100 μM sodium arsenite for 1 h. Cells were fixed and stained for eIF3b (red) and DAPI (blue) for stress granule analysis. Transfected cells were shown in green. Scale bar, 10 μm. **F** The GFP channel of panel **E** was used for quantifying stress granule number, mean area, and total area. The mean ± s.e. of each parameter was reported from three biological replicates; $^{**}p < 0.01$, $^{***}p < 0.001$, ns = not significant, two-tailed unpaired Mann–Whitney U test for SG number analysis and two-tailed unpaired Student's *t* test for the rest. Number of cells analyzed was provided in Source data.

https://doi.org/10.1038/s41467-024-55666-0

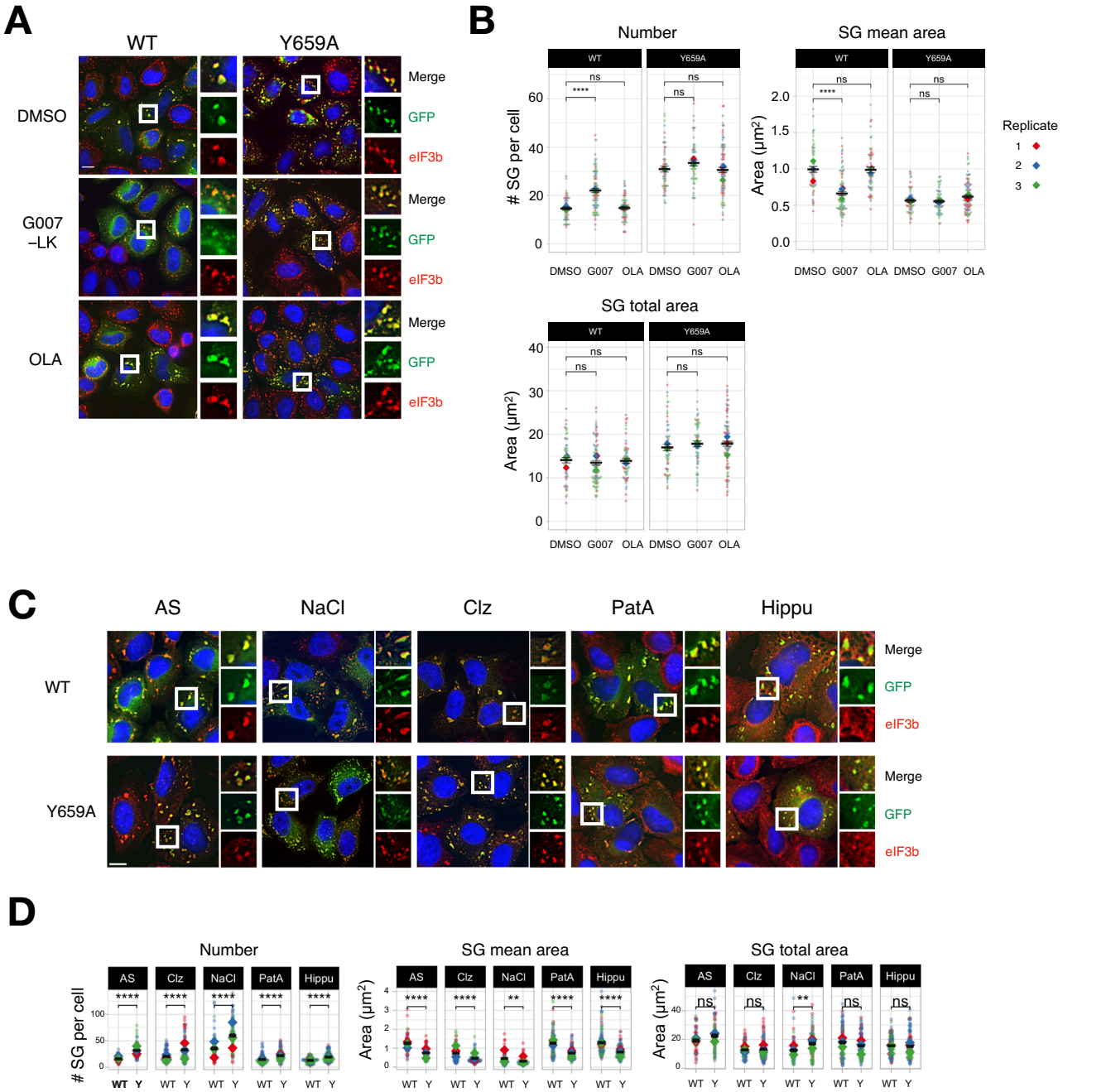

Fig. 3 | Cytoplasmic PAR regulates the formation of mature-sized stress granules. A HeLa PARP13 knockout cells transfected with GFP-PARP13.2 or Y659A were treated with PARP inhibitors (1 μM for G007-LK, 10 μM for Olaparib; OLA) for 30 min, followed by 250 μM sodium arsenite for an additional 30 min. Cells were fixed and stained for eIF3b (red) and DAPI (blue) for analyzing stress granules. Transfected cells were shown in green. Scale bar, 10 μm. **B** Quantification of panel **A**. GFP channel was used for quantifying stress granule number, mean area, and total area. The mean ± s.e. of each parameter was reported from three biological replicates; $^{****}p < 0.0001$, ns = not significant, two-tailed unpaired Mann–Whitney U test for SG number analysis and two-tailed unpaired Student's *t* test for the rest. Number of cells analyzed was provided in Source data. **C** HeLa PARP13 knockout cells expressing GFP-tagged wild-type PARP13.2 or Y659A mutant were treated with 100 μM sodium arsenite (AS), 200 mM sodium chloride (NaCl), 20 μM Clotrimazole (Clz), 100 nM Pateamine A (PatA), or 1 μM of Hippuristanol (Hippu) for 1 h. Cells were fixed and stained for eIF3b (red) and DAPI (blue) for stress granule analysis. Transfected cells were shown in green. Scale bar, 10 μm. **D** Quantification of panel **C**. GFP channel was used for quantifying stress granule number, mean area, and total area. The mean ± s.e. of each parameter was reported from three biological replicates; $^{**}p < 0.01$, $^{****}p < 0.0001$, ns = not significant, two-tailed unpaired Mann–Whitney U test for SG number analysis and two-tailed unpaired Student's *t* test for the rest. Number of cells analyzed was provided in Source data.

exhibited a greater number of stress granules that were smaller compared to the wild-type, as in the case of arsenite (Fig. 3C, D). Considering these stressors initiate stress granule formation via distinct pathways, these data indicate that although the PAR-binding activity of PARP13 regulates stress granule size and number, it is not required for initiating their formation.

The PAR-binding activity of PARP13 modulates stress granule fusion and disassembly

Given that the stress granules observed in cells expressing the Y659A mutant were smaller than those in wild-type cells when exposed to arsenite stress, as shown at the population level (Fig. 1F, G), we hypothesized that the Y659A mutant might impair stress granule fusion. To

https://doi.org/10.1038/s41467-024-55666-0

test this hypothesis, we carried out time-lapse cell imaging at the single-cell level to monitor stress granule assembly (Fig. 4A). We quantified the mean area of stress granules in HeLa PARP13 knockout cells reconstituted with wild-type PARP13.2 or the Y659A mutant at 30, 60, 90, and 120 min after arsenite treatment (Fig. S5A). At 30 min, small stress granules of similar size formed under both conditions. The stress granules in cells expressing the wild-type gradually increased in size after 60 min, consistent with previous studies on stress granule assembly[15,41]. In contrast, stress granules in cells expressing the Y659A mutant did not grow after 60 min.

Fig. 4 | PAR-binding ability of PARP13.2 governs the dynamics and liquid-like properties of stress granules. A HeLa PARP13 knockout cells expressing GFP-tagged wild-type PARP13.2 or Y659A mutant were treated with 100 μM sodium arsenite for time-lapse imaging. Snapshots were taken at indicated time points. Scale bar, 10 μm. **B** Fusion events were randomly chosen from time-lapsed images. The aspect ratio and circularity were measured at the 20th frame (1 min/frame) after fusion. Fusion events were analyzed from three biological replicates and the mean ± s.e. was indicated in the graph; ***$p < 0.001$, two-tailed unpaired Student's t test. The initial size of stress granules was measured from three biological replicates and displayed in violin plot. The embedded boxplots indicate median (middle line), 25th, 75th percentile (box) and 5th and 95th percentile (whiskers). Number of fusion events and cells analyzed were provided in Source data. **C** HeLa PARP13 knockout cells expressing GFP-tagged wild-type PARP13.2 or Y659A mutant were treated with 100 μM sodium arsenite for 1 h. Cells were rinsed and replenished with fresh medium for recovery. Cells were fixed after 0, 60, or 120 min, and stained for eIF3b (red) and DAPI (blue) to visualize stress granules. Transfected cells were shown in green. Scale bar, 10 μm. **D** Quantification of panel **C**. The percentage of stress granules in transfected cells were quantified at indicated time points from three biological replicates. The mean ± s.e. was indicated in the bar graph; *$p < 0.05$, **$p < 0.01$, ns = not significant, two-tailed unpaired Student's t test. Number of cells analyzed was provided in Source data. **E** GFP-tagged WT PARP13.2 or Y659A CRISPR knock-in HeLa cells were treated with 100 μM sodium arsenite. Stress granules were randomly selected 40 min–1.5 h post-treatment for FRAP analyses. Scale bar, 10 μm. **F** Quantification of panel **E**. An average of fluorescence intensity (intensity ± standard error) at each respective time point was plotted from three biological replicates. The number of granules analyzed for WT: $n = 22$; Y659A: $n = 22$. **G** FRAP analyses for mScarlet-UBAP2L CRISPR knock-in HeLa cells expressing GFP-PARP13.2 or Y659A mutant. Cells were treated with 100 μM sodium arsenite and stress granules were randomly selected 40 min–1.5 h post-treatment for FRAP analyses. Scale bar, 10 μm. **H** Quantification of panel **G**. An average of fluorescence intensity (intensity ± standard error) at each respective time point in each group was plotted from three biological replicates. The number of granules analyzed for WT: $n = 11$; Y659A: $n = 19$. **I** HeLa PARP13 knockout cells expressing GFP vector (Ctrl), GFP-tagged wild-type PARP13.2, or Y659A were treated with solvent control or 100 μM sodium arsenite for 1 h. Cells were lysed with 0.5% NP-40 containing buffer and centrifuged to separate soluble (supernatant) and insoluble (pellet) fractions. Samples were resolved by SDS-PAGE analysis. **J** Quantification of panel **I**. Intensity of GFP signals was normalized to loading control (Tubulin) and mock condition. The mean ± s.e. was reported from three biological replicates; *$p < 0.05$, ***$p < 0.001$, two-tailed unpaired Student's t test.

Next, we examined the actual stress granule fusion event, focusing on the relaxation behavior of fused condensates[42]. We randomly selected multiple fusion events from live cell imaging, tracking from the initial point of contact through 20 subsequent frames, at a rate of 1 min per frame. For each fusion event, we measured the initial granule size in cells expressing wild-type and Y659A mutant and quantified the aspect ratio and circularity of the fused condensate in the final frame (Fig. 4B). The premise is that if stress granules exhibit liquid-like properties, a fusion event followed by relaxation would manifest in a lower aspect ratio and a higher circularity. While stress granules in cells expressing wild-type PARP13 and the Y659A mutant had comparable initial size and fused over time, the aspect ratio and circularity measurement indicated that granules in cells expressing wild-type PARP13 relaxed closer to a spherical shape after fusion within 20 min (Fig. 4B). These data suggest that stress granules in cells expressing the PAR-binding deficient mutant displayed slower fusion kinetics compared to stress granules in cells expressing the wild-type.

Besides studying stress granule assembly, we investigated the impact of PARP13's PAR-binding ability on the disassembly of stress granules upon stress relief[41]. We treated PARP13 knockout cells, reconstituted either with wild-type PARP13.2 or the PAR-binding mutant, with arsenite. After removing the stress, we monitored stress granule disassembly for 2 h. After 1 h of stress removal, about 40% of stress granules in cells expressing the wild-type disassembled, while cells expressing the Y659A mutant retained stress granules at a similar level as observed during stress (Fig. 4C, D). This pattern persisted after 2 h of recovery, with 80% stress granules remaining in cells expressing the Y659A mutant, significantly higher than the 30% observed in wild-type. These data indicate that the PAR-binding ability of PARP13 is critical for controlling the rate of stress granule disassembly.

The PAR-binding activity of PARP13 modulates stress granule dynamics

Considering the impact of the PAR-binding mutant of PARP13 on reducing the fusion and disassembly of stress granules, we hypothesize that the constituent protein dynamics are reduced in stress granules. We performed fluorescence recovery after photobleaching (FRAP) analyses in PARP13 knockout cells, expressing either GFP-tagged wild-type PARP13.2 or the Y659A mutant. Wild-type PARP13 exhibited a significantly faster recovery and reached a higher steady-state level compared to the Y659A mutant (Fig. S5B). Given protein dynamics is sensitive to expression levels, we engineered a GFP-tag at the endogenous locus for expressing PARP13.2 and developed additional Y659A mutant cell lines via CRISPR-Cas9 (Fig. S5C). Prior to their use, we confirmed their edited gene sequences and protein expression (Fig. S5D, E). As expected, the CRISPR-engineered GFP-tagged Y659A cells exhibited a greater number of stress granules, which were noticeably smaller than those with the wild-type PARP13.2, upon arsenite treatment (Fig. S5F). The FRAP experiments revealed a consistent trend in dynamics as observed with the ectopically expressed system—namely, wild-type PARP13.2 displayed higher dynamics and a faster recovery rate than the Y659A mutant (Fig. 4E, F). Therefore, the PAR-binding deficiency not only modulates the size and number of stress granules but also reduces the dynamics of the PARP13 protein in stress granules.

To determine if the overall dynamics of stress granules were affected as well, we analyzed the recovery of the core stress granule marker UBAP2L[16]. In HeLa cells expressing mScarlet-tagged UBAP2L from the endogenous locus[16] and transfected with GFP-tagged PARP13.2 or the Y659A mutant, UBAP2L recovery was slower in the presence of the PAR-binding mutant compared to the wild-type (Figs. 4G, H, and S5G). These findings demonstrate that the PAR-binding activity of PARP13 modulates the dynamics of stress granule components.

Earlier studies have shown that the movement and fusion of stress granules follow microtubule dynamics[43,44]. Disrupting the dynamics of microtubules or microfilaments using chemical inhibitors[45,46], or genetic knockdown of microtubule scaffold proteins[47], result in smaller stress granules, underlining the crucial role of microtubules in stress granule maturation. However, no noticeable difference was found in microtubule staining between cells expressing the PARP13 Y659A mutant and those of the wild type (Fig. S5H), indicating the presence of an alternative regulatory mechanism affecting stress granule fusion.

Stress granules exhibit liquid-like properties[10], and the exchange of their constituents with the surrounding cytoplasm is influenced by the strength of the intermolecular protein interactions within the stress granules. We hypothesized that the reduced stress granules dynamics observed upon expression of the PARP13 PAR-binding mutant may be indicative of a more solid state. To test this hypothesis, we performed a solubility assay by transfecting HeLa PARP13 knockout cells with wild-type PARP13.2 or the Y659A mutant, treated them with arsenite for 1 h or left them untreated, and lysed the cells with detergent. We then separated cell lysates into soluble and insoluble fractions through centrifugation and analyzed the protein content by western blot. Consistent with our hypothesis, the Y659A mutant protein displayed greater insolubility than wild-type under arsenite treatment when stress granules were formed, whereas the solubility

was equivalent under unstressed conditions (Fig. 4I, J). This alteration in solubility, possibly reflecting a change in the physical state of the granules, may contribute to the observed impairment in stress granule fusion. Taken together, the PAR-binding activity of PARP13 is crucial for maintaining the dynamics and physical properties of stress granules, which is essential for their proper assembly and disassembly.

Cancer-associated PARP13 SNPs in WWE2 domain reduce PAR binding and result in fragmented stress granule phenotype

An examination of the COSMIC database[48] identified two cancer-associated SNPs, R681G and R681K, within the "PAR path" of PARP13 (Fig. 5A). This groove binds the extended portion of the polymer beyond the 2′ terminus of PAR at the WWE2 domain[30]. This discovery led us to hypothesize that these mutations reduce PAR binding and result in a fragmented stress granule phenotype, similar to that observed with the Y659A mutation (Fig. 1F, G). Despite the limited solubility of the R681G mutant impeding binding analyses, the R681K mutation demonstrated weaker in vitro binding to PAR compared to wild-type PARP13.2 (Fig. 5B). These mutants also exhibited fragmented stress granule phenotypes, characterized by a greater number of smaller-sized stress granules than those in the wild-type (Figs. 5C, D, and S6A). In contrast, the expression of another PARP13 SNP, E553V, which is distanced from the PAR path (Fig. 5A), did not reduce PAR binding (Fig. S6B) nor alter the number or size of stress granules (Fig. 5C, D).

Discussion

In this study, we have identified PARP13, specifically the PAR-binding activity of PARP13.2, as an important factor in regulating the dynamics and liquid-like properties of stress granules. Importantly, the loss of the PAR-binding activity of PARP13 not only reduces the dynamic properties of PARP13 itself but also lowers the dynamics of the core stress granule component UBAP2L. This change implies a shift in the dynamic behavior of the condensate per se. We show that the fusion frequency of the stress granules that form in the presence of the PAR-binding mutant of PARP13 is reduced and that their disassembly is delayed. Altogether, these data suggest that alterations of the molecular interactions within stress granules caused by the expression of the PARP13 mutant hinder the fusion of smaller condensates and result in a maturation defect.

PARP13 bridges molecular interaction networks within stress granules

PAR is critical for maintaining the structural integrity of stress granules[23,25], which is also exemplified by the mislocalization of many stress granule components when they lose their ability to bind to PAR[25,26]. Still, PAR may also play a broader role in preserving stress granule dynamics by modulating interactions amongst stress granule components. The PAR-binding mutant of PARP13 that still localizes to stress granules, likely via its RNA-binding domains, offers a unique tool to investigate the role of PAR in this context. By comparing data from RNA-binding and PAR-binding mutants, our results suggest that RNA is crucial for targeting PARP13 to stress granules, while the PAR-mediated interaction network is key to modulating stress granule size and dynamics. In this study, we uncovered several distinct characteristics:

First, the specific mode of PAR interaction is important for modulating stress granule properties. Adding one or more functional PARP13 WWE domain to the PAR-binding mutant partially restores the size of stress granules. In contrast, the addition of the WWE domain of RNF146, which recognizes the bridging unit instead of the 2′ end of PAR, is unable to compensate. These findings highlight the sensitivity of the interaction network to the configuration of the PAR-binding site within PARP13 and its specific mode of interaction with PAR.

Second, our data demonstrate that losing the PAR interaction of a single stress granule component, PARP13, is sufficient to alter stress granule properties, despite the continued presence of PAR. Notably, the cancer-associated SNP R681K, which exhibits only a partial reduction in PAR-binding (threefold weaker than wild type), induces this phenotype. This finding suggests that the disruption of stress granule assembly by PARP13 does not require an almost complete PAR-binding deficiency, as seen with the W611A, Q668A, and Y659A mutants, but rather a reduction beyond a critical threshold. While we cannot entirely rule out other functions of the WWE domain, the fact that four distinct binding-pocket mutations—each impairing PAR-binding—produce the same phenotype underscores the critical role of PAR-binding in maintaining the proper size and assembly of stress granules.

PARP13 is part of a growing class of proteins that can bind both PAR and RNA[29,30,32,35,49]—two chemically similar yet functionally distinct nucleic acids integral to stress granule integrity. This dual-binding capability may facilitate condensate formation by linking various interaction networks (Fig. 5E). Effectively, PARP13 proteins act as hubs that connect existing protein-RNA and RNA-RNA interactions to PARylated proteins (e.g., the core components G3BP1 and G3BP2[23,50]). Since PAR is a post-translational modification that can be instantaneously added to proteins during stress, PARP13 can amplify the potential for multivalency connecting through the PAR interactome to the existing RNA interactome, forming mature-sized stress granules (Fig. 5E). Conversely, the loss of PARP13 or PARP5a activity results in smaller stress granules due to the loss of this hub or the connecting polymer, respectively (Fig. S6C, D).

Such a dual-binding capability of PARP13 may also suggest a scenario where mutants incapable of binding to PAR could still occupy RNA binding sites (Fig. S6E). This mutant occupancy could effectively prevent the wild-type proteins from functioning, potentially leading to the observed dominant-negative fragmented phenotype in stress granules.

Lastly, this crosstalk might also be crucial in determining the physical properties of the resulting granules. In support of this notion, our previous work demonstrated that modulating the ratio of RNA and PAR can influence the physical size and dynamics of FUS condensates in vitro[51]. In addition, a recent study demonstrated that PAR prevents apoptosis signal-regulating kinase 3 (ASK3) from forming solid-like condensates in vitro and increases the dynamic exchange of this kinase from condensates to surrounding cytoplasm in cells[52].

Physiological, pathological, and therapeutical implications of PAR–protein interactions

Mutations in stress granule proteins that reduce protein dynamics in vitro are often implicated in liquid-to-solid transitions and aggregate formation, which is a characteristic of many neurodegenerative diseases[2,3,11,21,22]. It has been difficult to investigate this phenomenon directly in cells since it is not easy to differentiate between the direct effects of mutations on protein function and their impact on granule properties. Our study uncovers the PARP13 PAR-binding deficient mutant as a potential research tool to determine whether shifts in the physical properties of stress granules amplify toxicity in cellular and animal models of neurodegenerative diseases, especially given its dominant-negative effect.

Our study also identified two cancer-associated SNPs within the PAR-binding region, resulting in the fragmented stress granule phenotype. Given that recent data establish a causal relationship between stress granules and certain cancers[53,54], the PAR-binding activity of PARP13 might contribute to cancer pathogenesis, warranting further investigation.

Beyond implications for neurodegeneration and cancer, PARP13—also known as the zinc finger antiviral protein (ZAP)—plays a notable role in antiviral defense[29,33,55,56] and localizes to stress granules during viral infections[34]. Curiously, mutations in its PAR-binding site reduce the activity of PARP13 against retroviruses, such as HIV-1 and murine leukemia virus[29], but confer antiviral activity against alphaviruses, such

https://doi.org/10.1038/s41467-024-55666-0

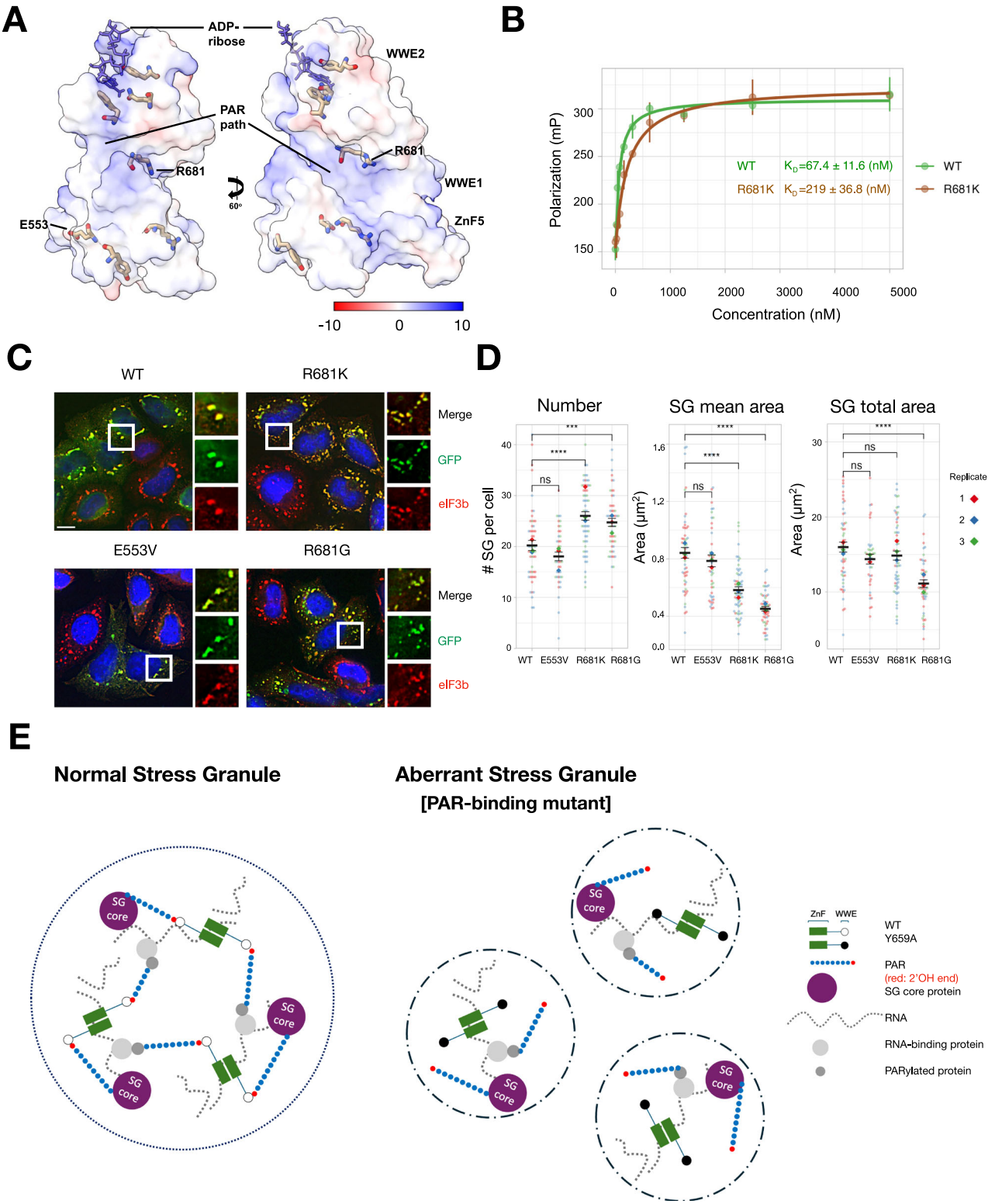

Fig. 5 | PAR-binding deficient cancer SNPs of PARP13 exhibit smaller and more numerous stress granules. A Structural model of PARP13.2-WWE domains (PDB: 7TGQ). The positively charged surface highlighted in blue indicates the potential "PAR path" that stabilizes PAR-binding. **B** ZnF5-WWE1&2 protein fragments of wild-type PARP13.2 or R681K mutant were incubated with 20-mer FAM-PAR to examine protein-PAR binding by fluorescence polarization. The mean ± SD was reported from three biological replicates; $p < 0.005$; two-tailed unpaired Student's *t*-test. **C** Wild-type HeLa cells expressing GFP-tagged wild-type or mutant PARP13.2 constructs were treated with 250 μM sodium arsenite for 30 min. Cells were fixed and stained for eIF3b (red) and DAPI (blue). Transfecetd cells were shown in green. Scale bar, 10 μm. **D** Quantification of panel **C**. GFP channel was used to quantify stress granule number, mean area, and total area. The mean ± s.e. of each parameter was reported from three biological replicates; ***$p < 0.001$, ****$p < 0.0001$, ns = not significant, two-tailed unpaired Mann–Whitney U test for SG number analysis and two-tailed unpaired Student's *t* test for the rest. Number of cells analyzed was provided in Source data. **E** Working model: The dual-binding ability of PARP13 allows it to act as a hub of multivalent interactions, linking the PAR interactome (PARylated proteins and PAR-binding proteins) with the RNA interactome (RNA-binding proteins and RNA-RNA interactions) in addition to protein-protein interactions. Notably, stress granule core components such as G3BP1, G3BP2 and UBAP2L are ADP-ribosylated[64], and G3BP1 and G3BP2 bind to PAR[50].

as Sindbis virus[57]. This raises the intriguing possibility that PARP13's antiviral function could also be influenced by changes in the size and number of stress granules.

Besides stress granules, PAR enrichment has been observed in other condensates such as nucleoli, DNA damage repair foci, and mitotic spindles, all of which have potential implications in cancer[58]. With almost 2000 PAR-binding proteins identified in proteomics studies[59–63], we are poised to make substantial progress in understanding PAR-mediated protein interaction networks. Our study underscores the importance of characterizing PAR-binding sites and studying the effects of binding-deficient mutants in live cells and tissues, because their identifications will offer invaluable insights into the biological roles of PAR-protein interactions. Therapeutic targeting of these interactions may open avenues in disease treatments.

Methods

Constructs

Various PARP13 deletion, mutant, and chimera constructs were generated by PCR and confirmed by sequencing.

Cell culture and chemical treatment. Cell lines, including HeLa (Kyoto), HeLa PARP13 knockout (Kyoto)[32], U2OS, CRISPR-engineered PARP13 HeLa (Kyoto), mScarlet UBAP2L HeLa cells were maintained in DMEM supplemented with 10% fetal bovine serum and cultured at 37 °C and 5% CO_2 in a humidified incubator. PARP inhibitors were dissolved in DMSO. Cells were treated with indicated concentration of inhibitors for 30 min (1 μM G007-LK; 10 μM Olaparib; 10 μM XAV939; 5 μM TA-91; 5 μM TA-92), then treated with 250 μM sodium arsenite in the presence of the inhibitors for another 30 min. Various stressors were treated after 24 h of transfection for 1 h unless otherwise indicated (100 μM sodium arsenite; 200 mM NaCl; 20 μM Clotrimazole; 1 μM Hippuristanol; 100 nM Pateamine A).

Endogenous-tagging cells by CRISPR/Cas9 system. CRISPR GFP-knock-in cells were performed as per the manufacturer's instruction (TrueTag™ Donor DNA kit, Invitrogen). Briefly, a donor DNA template with C-terminal GFP and homologous arms was prepared by PCR. gRNA was prepared by PCR followed by in vitro transcription (TranscriptAid T7 High Yield Transcription kit, Invitrogen). Donor template, gRNA, and Cas9 were transfected to the HeLa (Kyoto) cells by lipofectamine-3000. After two days, cells were treated with blasticidine. Single clones were obtained by FACS sorting. Gene editing was validated by junction-PCR, western blot, and Sanger sequencing. For the Y659A mutant cell line, donor DNA templates with site mutation were ordered from IDT. Editing efficiency was compared among three sets of gRNA and donor templates by T7E1 cleavage assay, and the best pair was selected. After transfecting the DNA donor template, gRNA, and Cas9 to GFP-PARP13.2 HeLa cells, serial dilution was performed to obtain single clones. Potential mutant clones were screened by restriction enzyme, Bsp 1286I, and then confirmed by TOPO cloning and sequencing.

Transfection and immunofluorescence. 2.5×10^5 cells were seeded in 6-well plates with sterilized glass coverslips. After 24 h, 1 μg plasmid was transfected to each well by lipofectamine-2000 for 24 h. Cells were mock-treated or treated with 100 μM sodium arsenite for 1 h. Cells were rinsed three times with PBS, then fixed with 4% paraformaldehyde (PFA) in PBS for 10 min. Cells were permeabilized by 0.1% Triton-X-100 for 10 min, followed by three times PBS wash. Coverslips were blocked by blocking buffer (5% normal horse serum in PBS) for 15 min and were incubated with primary antibodies for 1 h. Coverslips were washed by PBST (PBS containing 0.1% Tween-20) three times and incubated with fluorescence-tagged secondary antibodies for 45 min. Coverslips were washed by PBST three times. Nucleus was stained wtih 0.01% DAPI for 1 min. Coverslips were quickly rinsed three times by PBS, and the residual buffer was removed before mounting (ProLong Gold). Images were acquired by DeltaVision Elite microscope equipped with a 60X (NA 1.42 with 1.516 oil) objective, a DAPI/FITC/TRITC/Cy5 filter set, and a high-speed CCD camera (Cool SNAP HQ^2). Experiments were controlled and recorded by SoftWorx (GE Healthcare).

Stress granule quantitation. For each experimental condition, more than five images comprising 21 Z-sections (size = 0.2 μm) were taken. Focused z-layer was selected from each image and exported as a tiff file for ImageJ analysis. The images were processed by macros to increase signal-to-background ratio. The channel of GFP (transfected cells) or Cy5 was used for stress granule quantitation. The proper threshold (Otsu) and watershed were manually set to cover all granules in the field with appropriate resolution. DAPI channel was used for nucleus quantitation, and the corresponding cytoplasmic area was circled by freehand selection tool as the region-of-interests (ROIs) and were added to ROI manager. The function "Analyze particles" was used to measure the nucleus area, stress granule number per cell, average stress granule area per cell, and total stress granule area per cell. Each condition was analyzed from at least three biological replicates, with 50–150 cells analyzed. All graphs were made by ggplot2 (RStudio) and shown by mean ± standard error.

Time-lapse cell imaging. Cells were seeded in 4-well Chambered coverglass (Nunc™, Lab-Tek™ II, 1.5 borosilicate glass) and transfected with GFP-tagged PARP13.2 or Y659A mutant. Before 1 h of the experiment, cells were kept at 37 °C, 5% CO_2, humidified environment to ensure the cells were in equilibrium with the setting of the microscope. Images were acquired by DeltaVision Elite system (GE Healthcare) microscope equipped with a 60X (NA 1.42 with 1.520 oil) objective. SoftWorx was used to control and set the conditions. Around ten Z-stacks (each stack = 0.4 μm) were set to cover the whole volume of the cell. Images were taken at 1-min intervals. After 5 images, sodium arsenite was applied at the final concentration of 100 μM and the imaging would be continued for 2 h. Before quantitation, images were maximally projected and processed by ImageJ. The setting of threshold of stress granules was identical as previously described in *"stress granule quantitation"*. Around 15–20 cells of each condition were analyzed. The graph was made by ggplot2 (RStudio).

Fluorescence recovery after photobleaching (FRAP). Cells were seeded in 4-well Chambered coverglass and were mock-treated or 100 μM sodium arsenite treated. Cells were maintained at 37 °C, 5% CO_2, humidified environment during the experiment, and images were obtained on a single focal plane by confocal microscope (Zeiss LSM800 GaAsP) equipped with 63X/1.4 Oil DIC M27 PlanApo objective. ZEN (Zeiss) was used to obtain and record data. Two stress granules were selected from the same cell, one for bleaching, and the other one for reference. Two identical sizes of squares were drawn as region-of-interests (ROIs) to cover the stress granule areas. For CRISPR GFP-knock-in cells, photobleaching was set with 100% 488 nm laser on ROIs (Scan speed = 7) and images were acquired every 1.5 s. Five images of each stress granule were taken before bleaching. The area was bleached for 5 iterations, and the mean fluorescence intensity was recorded for 5 min. To ensure the bleaching is equally effective among different ROIs, we only analyzed the ones that have around 10% fluorescence intensity remaining after bleaching. The mean intensity of fluorescence and curve fitting was analyzed by ImageJ. Briefly, all intensity of ROIs was substrated from the background first. ROIs of bleached or referenced granules were normalized to the averaged five measurements before bleaching individually. Values of bleached ROIs were normalized again to referenced ROIs, the values were then used

for exponential recovery curve fitting. Mobility and T-half were obtained as follows:

$$y = a \times [1 - e^{-bx}] + c \quad (1)$$

$$Mobility = \frac{a}{1 - c} \quad (2)$$

$$t_{\frac{1}{2}} = b \times \ln 2 \quad (3)$$

For mScarlet-UBAP2L cells, photobleaching was set with 50% 561 nm and 488 nm laser on ROIs (Scan speed = 7). Otherwise, the settings were identical to the above. We monitored both fluorescence channels to ensure that the bleaching levels were similar between wild-type and mutant PARP13.2 transfected cells. Each condition was analyzed in biological triplicates, with around 15–20 cells, and the graph was made by ggplot2.

Solubility assay. HeLa PARP13 knockout cells expressing GFP-tagged vector, PARP13.2, or PARP13.2-Y659A mutant were cultured in 6-well plates. After 24 h, cells were mock-treated or treated with 100 μM sodium arsenite for 1 h. Cells were washed three times, scraped down with cold PBS, and spun down to collect the pellet. 50 μL lysis buffer (50 mM Tris pH 8.8, 100 mM NaCl, 5 mM $MgCl_2$, 0.5% NP-40, 2 mM DTT, 1 mM PMSF, 1X cOmplete EDTA-free protease inhibitor cocktail (Roche), 1X PhosSTOP (Roche), 1 μM Olaparib, 1 μM PDDX) was added to resuspend the pellets. Samples were kept on ice for 20 min and centrifuged at 18,000 × *g* at 4 °C for 15 min. The supernatant was transferred to new tubes as soluble fraction. For the remaining pellet, 20 μL 1X protein sample buffer (60 mM Tris pH 6.8, 4% SDS, 10% glycerol, 5% β-mercaptoethanol, 3 μg/mL bromophenol blue) was added for resuspension. The samples were vortexed and boiled at 95 °C for 10 min for insoluble fraction.

Puromycin assay and Western blot. Cells were mock-treated or treated with 100 μM sodium arsenite for 1 h. Puromycin was added into the medium before 20 min of harvest (final concentration of 100 μg/mL). Cells were rinsed twice with cold PBS, and 1X protein sample buffer was added to harvest the cells. The samples were boiled at 95 °C for 10 min for PAGE analyses. Samples were transferred to nitrocellulose membrane by semi-dry transfer (300 mA, 1 h). Membranes were blocked by TBST (TBS + 0.15% Tween-20) containing 4% skimmed milk for 30 min, followed by incubation in primary antibody diluted by 5% BSA in TBST at cold room overnight. Membranes were washed for 5 min in TBST three times and incubated with corresponding fluorophore-conjugated secondary antibody (1:20,000) at room temperature for 30 min. Membranes were washed another three times for 5 min each in TBST, and images were acquired by Odyssey imager (Li-COR Biosciences).

Fluorescence polarization. Experiments were performed as previously published[30]. Briefly, 20-mer PAR was labeled with FAM at 1"-end. The labeled probe was incubated with indicated concentrations of proteins in 12 mM HEPES (pH 8.0), 25 mM KCl, 50 μg/mL BSA, 4% glycerol, and 0.1 mM TECP at room temperature for 30 min. Fluorescence polarization measurements were done on a Victor3V plate reader (PerkinElmer). Measurements were obtained by subtracting the values from buffer conditions. For binding curves, the data were fit with nonlinear regression to obtain binding constant (K_D) values. The graph was made by hyperbola formula, providing the average K_D value, standard deviation, maximum and minimum values acquired from triplicated measurements.

PAR staining and colocalization analysis. 2.5×10^5 CRISPR-engineered wild-type or Y659A cells were seeded in 6-well plates with sterilized glass coverslips. After 48 h, the cells were treated with 250 μM sodium arsenite for 1 h. The cells were rinsed three times with PBS and then fixed with ice-cold methanol for 5 min at −20 °C. PBS was added sequentially to dilute the methanol concentration by half each time, for a total of three dilutions, followed by three PBS wash. Coverslips were blocked with blocking buffer for 20 min and incubated with primary antibodies (1:50) at 4 °C overnight. The remaining steps were identical to those described in "*Transfection and Immunofluorescence*". Colocalization analysis was performed based on the GFP channel, where equal-sized squares were set as regions of interest (ROIs) to cover areas of background or stress granules, which were then added to the ROI manager. The BIOP JAcoP plug-in in ImageJ was used to manually set the threshold for each channel and perform the analysis to measure the correlation of PAR signals with the specified areas. Pearson correlation coefficients for each area were obtained and pooled from 2–3 biological replicates. Data were graphed using ggplot2 (RStudio) and presented as mean ± standard error.

Statistics and Reproducibility. All the experiments in this study were conducted using biological triplicates independently. The number of cells or granules analyzed is listed in Source data. Data are presented as mean ± standard error or mean ± standard deviation, as noted in the legend. For the analysis of stress granule numbers, groups were compared using a two-tailed unpaired Mann–Whitney U test. For the remaining analyses, groups were compared using a two-tailed unpaired Student's *t*-test. Adjusted *p*-values were applied for multiple comparasions. All statistical analyses were performed using RStudio.

Reporting summary

Further information on research design is available in the Nature Portfolio Reporting Summary linked to this article.

Data availability

Data supporting this finding are available within the main text, Supplementary Figs. and tables, and Source data. Source data are provided with this paper.

References

1. Glauninger, H., Wong Hickernell, C. J., Bard, J. A. M. & Allan Drummond, D. Stressful steps: progress and challenges in understanding stress-induced mRNA condensation and accumulation in stress granules. *Mol. Cell* **82**, 2544–2556 (2022).
2. Fakim, H. & Vande Velde, C. The implications of physiological biomolecular condensates in amyotrophic lateral sclerosis. *Semin. Cell Dev. Biol.* https://doi.org/10.1016/j.semcdb.2023.05.006 (2023).
3. Ramaswami, M., Taylor, J. P. & Parker, R. Altered ribostasis: RNA-protein granules in degenerative disorders. *Cell* **154**, 727–736 (2013).
4. Hofmann, S., Kedersha, N., Anderson, P. & Ivanov, P. Molecular mechanisms of stress granule assembly and disassembly. *Biochim. Biophys. Acta Mol. Cell Res.* **1868**, 118876 (2021).
5. Eiermann, N., Haneke, K., Sun, Z., Stoecklin, G. & Ruggieri, A. Dance with the devil: stress granules and signaling in antiviral responses. *Viruses* **12**, 984 (2020).
6. Millar, S. R. et al. A new phase of networking: the molecular composition and regulatory dynamics of mammalian stress granules. *Chem. Rev.* https://doi.org/10.1021/acs.chemrev.2c00608 (2023).
7. Kedersha, N. L. & Anderson, P. Mammalian stress granules and processing bodies. *Methods Enzymol.* **431**, 61–81 (2007).
8. Baymiller, M. & Moon, S. L. Stress granules as causes and consequences of translation suppression. *Antioxid. Redox Signal.* https://doi.org/10.1089/ars.2022.0164 (2023).

9. Lin, Y., Protter, D. S. W., Rosen, M. K. & Parker, R. Formation and maturation of phase-separated liquid droplets by RNA-binding proteins. *Mol. Cell* **60**, 208–219 (2015).
10. Molliex, A. et al. Phase separation by low complexity domains promotes stress granule assembly and drives pathological fibrillization. *Cell* **163**, 123–133 (2015).
11. Patel, A. et al. A liquid-to-solid phase transition of the ALS protein FUS accelerated by disease mutation. *Cell* **162**, 1066–1077 (2015).
12. Wippich, F. et al. Dual specificity kinase DYRK3 couples stress granule condensation/dissolution to mTORC1 signaling. *Cell* **152**, 791–805 (2013).
13. Wheeler, J. R., Matheny, T., Jain, S., Abrisch, R. & Parker, R. Distinct stages in stress granule assembly and disassembly. *eLife* **5**, 875 (2016).
14. Buchan, J. R. & Parker, R. Eukaryotic stress granules: the ins and outs of translation. *Mol. Cell* **36**, 932–941 (2009).
15. Kedersha, N. L. et al. Dynamic shuttling of TIA-1 accompanies the recruitment of mRNA to mammalian stress granules. *J. Cell Biol.* **151**, 1257–1268 (2000).
16. Cirillo, L. et al. UBAP2L forms distinct cores that act in nucleating stress granules upstream of G3BP1. *Curr. Biol.* https://doi.org/10.1016/j.cub.2019.12.020 (2020).
17. Matsuki, H. et al. Both G3BP1 and G3BP2 contribute to stress granule formation. *Genes Cells* **18**, 135–146 (2013).
18. Kedersha, N. L. et al. G3BP-Caprin1-USP10 complexes mediate stress granule condensation and associate with 40S subunits. *J. Cell Biol.* **212**, 845–860 (2016).
19. Fang, M. Y. et al. Small-molecule modulation of TDP-43 recruitment to stress granules prevents persistent TDP-43 accumulation in ALS/FTD. *Neuron* **103**, 802–819.e11 (2019).
20. Yang, P. et al. G3BP1 is a tunable switch that triggers phase separation to assemble stress granules. *Cell* **181**, 325–345.e28 (2020).
21. Alberti, S. & Dormann, D. Liquid-liquid phase separation in disease. *Annu. Rev. Genet*. https://doi.org/10.1146/annurev-genet-112618-043527 (2019).
22. Mathieu, C., Pappu, R. V. & Taylor, J. P. Beyond aggregation: pathological phase transitions in neurodegenerative disease. *Science* **370**, 56–60 (2020).
23. Leung, A. K. L. et al. Poly(ADP-ribose) regulates stress responses and microRNA activity in the cytoplasm. *Mol. Cell* **42**, 489–499 (2011).
24. Catara, G. et al. PARP1-produced poly-ADP-ribose causes the PARP12 translocation to stress granules and impairment of Golgi complex functions. *Sci. Rep.* **7**, 14035 (2017).
25. Duan, Y. et al. PARylation regulates stress granule dynamics, phase separation, and neurotoxicity of disease-related RNA-binding proteins. *Cell Res.* **29**, 233–247 (2019).
26. McGurk, L. et al. Poly(ADP-Ribose) prevents pathological phase separation of TDP-43 by promoting liquid demixing and stress granule localization. *Mol. Cell* **71**, 703–717.e9 (2018).
27. Leung, A. K. L. Poly(ADP-ribose): an organizer of cellular architecture. *J. Cell Biol.* **205**, 613–619 (2014).
28. Rhine, K., Odeh, H. M., Shorter, J. & Myong, S. Regulation of biomolecular condensates by poly(ADP-ribose). *Chem. Rev.* https://doi.org/10.1021/acs.chemrev.2c00851 (2023).
29. Xue, G. et al. Poly(ADP-ribose) potentiates ZAP antiviral activity. *PLoS Pathog.* **18**, e1009202 (2022).
30. Kuttiyatveetil, J. R. A. et al. Crystal structures and functional analysis of the ZnF5-WWE1-WWE2 region of PARP13/ZAP define a distinctive mode of engaging poly(ADP-ribose). *Cell Rep.* **41**, 111529 (2022).
31. Charron, G., Li, M. M. H., Macdonald, M. R. & Hang, H. C. Prenylome profiling reveals S-farnesylation is crucial for membrane targeting and antiviral activity of ZAP long-isoform. *Proc. Natl. Acad. Sci. USA.* **110**, 11085–11090 (2013).
32. Todorova, T., Bock, F. J. & Chang, P. PARP13 regulates cellular mRNA post-transcriptionally and functions as a pro-apoptotic factor by destabilizing TRAILR4 transcript. *Nat. Commun.* **5**, 5362 (2014).
33. Busa, V. F. et al. Transcriptome regulation by PARP13 in basal and antiviral states in human cells. *iScience* **27**, 109251 (2024).
34. Law, L. M. J. et al. ZAP's stress granule localization is correlated with its antiviral activity and induced by virus replication. *PLoS Pathog.* **15**, e1007798 (2019).
35. Chen, S. et al. Structure of N-terminal domain of ZAP indicates how a zinc-finger protein recognizes complex RNA. *Nat. Struct. Mol. Biol.* **19**, 430–435 (2012).
36. Wang, Z. et al. Recognition of the iso-ADP-ribose moiety in poly(-ADP-ribose) by WWE domains suggests a general mechanism for poly(ADP-ribosyl)ation-dependent ubiquitination. *Genes Dev.* **26**, 235–240 (2012).
37. Lüscher, B. et al. ADP-ribosyltransferases, an update on function and nomenclature. *FEBS J.* https://doi.org/10.1111/febs.16142 (2021).
38. Haikarainen, T., Krauss, S. & Lehtio, L. Tankyrases: structure, function and therapeutic implications in cancer. *Curr. Pharm. Des.* **20**, 6472–6488 (2014).
39. Huang, S.-M. A. et al. Tankyrase inhibition stabilizes axin and antagonizes Wnt signalling. *Nature* **461**, 614–620 (2009).
40. Nathubhai, A. et al. Highly potent and isoform selective dual site binding tankyrase/Wnt signaling inhibitors that increase cellular glucose uptake and have antiproliferative activity. *J. Med. Chem.* **60**, 814–820 (2017).
41. Kedersha, N. L., Tisdale, S., Hickman, T. & Anderson, P. Real-time and quantitative imaging of mammalian stress granules and processing bodies. *Methods Enzymol.* **448**, 521–552 (2008).
42. Kroschwald, S. et al. Promiscuous interactions and protein disaggregases determine the material state of stress-inducible RNP granules. *eLife* **4**, e06807 (2015).
43. Chernov, K. et al. Role of microtubules in stress granule assembly: Microtubule dynamical instability favors the formation of micrometric stress granules in cells. *J. Biol. Chem.* **284**, 36569–36580 (2009).
44. Nadezhdina, E. S., Lomakin, A. J., Shpilman, A. A., Chudinova, E. M. & Ivanov, P. A. Microtubules govern stress granule mobility and dynamics. *Biochim. Biophys. Acta* **1803**, 361–371 (2010).
45. Ivanov, P. A., Chudinova, E. M. & Nadezhdina, E. S. Disruption of microtubules inhibits cytoplasmic ribonucleoprotein stress granule formation. *Exp. Cell Res.* **290**, 227–233 (2003).
46. Loschi, M., Leishman, C. C., Berardone, N. & Boccaccio, G. L. Dynein and kinesin regulate stress-granule and P-body dynamics. *J. Cell Sci.* **122**, 3973–3982 (2009).
47. Kolobova, E. et al. Microtubule-dependent association of AKAP350A and CCAR1 with RNA stress granules. *Exp. Cell Res.* **315**, 542–555 (2009).
48. Forbes, S. A. et al. COSMIC: somatic cancer genetics at high-resolution. *Nucleic Acids Res.* **45**, D777–D783 (2017).
49. Busa, V. F. et al. Transcriptome regulation by PARP13 in basal and antiviral states in human cells. *iScience* **27**, 109251 (2022).
50. Jayabalan, A. K. et al. Stress granule formation, disassembly, and composition are regulated by alphavirus ADP-ribosylhydrolase activity. *Proc. Natl. Acad. Sci. USA.* **118**, e2021719118 (2021).
51. Rhine, K. et al. Poly(ADP-ribose) drives condensation of FUS via a transient interaction. *Mol. Cell* **82**, 969–985.e11 (2022).
52. Watanabe, K. et al. Cells recognize osmotic stress through liquid–liquid phase separation lubricated with poly(ADP-ribose). *Nat. Commun.* **12**, 1353 (2021).
53. Fonteneau, G. et al. Stress granules determine the development of obesity-associated pancreatic cancer. *Cancer Discov*. https://doi.org/10.1158/2159-8290.CD-21-1672 (2022).
54. Grabocka, E. & Bar-Sagi, D. Mutant KRAS enhances tumor cell fitness by upregulating stress granules. *Cell* **167**, 1803–1813.e12 (2016).

55. Schwerk, J. et al. RNA-binding protein isoforms ZAP-S and ZAP-L have distinct antiviral and immune resolution functions. *Nat. Immunol.* https://doi.org/10.1038/s41590-019-0527-6 (2019).
56. Gao, G., Guo, X. & Goff, S. P. Inhibition of retroviral RNA production by ZAP, a CCCH-type zinc finger protein. *Science* **297**, 1703–1706 (2002).
57. Huang, S. et al. Positive selection analyses identify a single WWE domain residue that shapes ZAP into a more potent restriction factor against alphaviruses. *PLoS Pathog.* **20**, e1011836 (2024).
58. Leung, A. K. L. Poly(ADP-ribose): a dynamic trigger for biomolecular condensate formation. *Trends Cell Biol.* **30**, 370–383 (2020).
59. Dasovich, M. & Leung, A. K. L. PARPs and ADP-ribosylation: deciphering the complexity with molecular tools. *Mol. Cell* **83**, 1552–1572 (2023).
60. Dasovich, M. et al. Identifying poly(ADP-ribose)-binding proteins with photoaffinity-based proteomics. *J. Am. Chem. Soc.* **143**, 3037–3042 (2021).
61. Kliza, K. W. et al. Reading ADP-ribosylation signaling using chemical biology and interaction proteomics. *Mol. Cell* **81**, 4552–4567 (2021).
62. Lam, A. T. et al. A bifunctional NAD+ for profiling poly-ADP-ribosylation-dependent interacting proteins. *ACS Chem. Biol.* https://doi.org/10.1021/acschembio.0c00937 (2021).
63. Kang, B. G. et al. Proteome-wide microarray-based screening of PAR-binding proteins. Preprint at *bioRxiv* https://www.biorxiv.org/content/10.1101/2022.06.06.494829v1 (2022).
64. Ayyappan, V. et al. ADPriboDB 2.0: an updated database of ADP-ribosylated proteins. *Nucleic Acids Res.* **49**, D261–D265 (2021).

Acknowledgements

We thank Drs. Phillip Sharp, Geraldine Seydoux, Michael Matunis, Valeria Culotta, Bin Wu, Danfeng Cai, Tatjana Trcek, Lyle McPherson, and the members of the Leung lab for their candid critiques on this work. We thank Dr. Paul Chang for sharing PARP13 plasmids and HeLa (Kyoto) PARP13 wild-type and knockout cells, Dr. Monica Gotta for sharing the mScarlet-UBAP2L HeLa cells, Dr. Amit Nathubhai for sharing chemical inhibitors TA91 and TA92, Dr. Zan Chen for technical support on CRISPR, Dr. Danfeng Cai for advising stress granule fusion quantification. This work was supported by NIH grant R01GM104135 (A.K.L.L), Ministry of Education Scholarship from Taiwan (S.-J.C.) and Brian Crawford Award (S.-J.C.) as well as Start-up fund (A.K.L.L.) from Johns Hopkins Bloomberg School of Public Health.

Author contributions

Conceptualization: S.-J.C. and A.K.L.L. Formal analysis: S.-J.C., T.G., J.R.A.K., and A.S. Investigation: S.-J.C., T.G., C.C., J.R.A.K., and A.S. Methodology: S.-J.C., J.R.A.K., and A.S. Resources: S.-J.C., J.R.A.K., and A.S. Validation: M.X. and A.L. Visualization: S.-J.C., J.R.A.K., and A.S. Writing – original draft: A.K.L.L. and S.-J. C. Writing – review & editing: A.K.L.L., S.-J.C., J.M.P., J.R.A.K., and A.S. Supervision: A.K.L.L. and J.M.P. Funding acquisition: A.K.L.L.

Competing interests

The authors declare no competing interests.

Additional information

Supplementary information The online version contains supplementary material available at https://doi.org/10.1038/s41467-024-55666-0.

Correspondence and requests for materials should be addressed to Anthony K. L. Leung.

Peer review information *Nature Communications* thanks the anonymous reviewers for their contribution to the peer review of this work. A peer review file is available.